ORIGINAL PAPER

Computational and experimental investigation of local stress fiber orientation in uniaxially and biaxially constrained microtissues

**Christine Obbink-Huizer · Jasper Foolen · Cees W. J. Oomens · Michael Borochin ·
Christopher S. Chen · Carlijn V. C. Bouten · Frank P. T. Baaijens**

Abstract The orientation of cells and associated F-actin stress fibers is essential for proper tissue functioning. We have previously developed a computational model that qualitatively describes stress fiber orientation in response to a range of mechanical stimuli. In this paper, the aim is to quantitatively validate the model in a static, heterogeneous environment. The stress fiber orientation in uniaxially and biaxially constrained microscale tissues was investigated using a recently developed experimental system. Computed and experimental stress fiber orientations were compared, while accounting for changes in orientation with location in the tissue. This allowed for validation of the model, and additionally, it showed how sensitive the stress fiber orientation in the experimental system is to the location where it is measured, i.e., the heterogeneity of the stress fiber orientation. Computed and experimental stress fiber orientations showed good quantitative agreement in most regions. A strong local alignment near the locations where boundary conditions were enforced was observed for both uniaxially and biaxially constrained tissues. Excepting these regions, in biaxially constrained tissues, no preferred orientation was found and the distribution was independent of location. The stress fiber orientation in uniaxially constrained tissues was more heterogeneous, and stress fibers mainly oriented in the constrained direction or along the free edge. These results indicate that the stress fiber orientation in these constrained microtissues is mainly determined by the local mechanical environment, as hypothesized in our model, and also that the model is a valid tool to predict stress fiber orientation in heterogeneously loaded tissues.

C. Obbink-Huizer (✉) · J. Foolen · C. W. J. Oomens ·
C. V. C. Bouten · F. P. T. Baaijens
Department of Biomedical Engineering, Eindhoven University
of Technology, PO Box 513, 5600 MB Eindhoven, The Netherlands
e-mail: c.obbink@tue.nl

M. Borochin · C. S. Chen
Department of Bioengineering, University of Pennsylvania,
510 Skirkanich Hall, 220 S. 33rd St, Philadelphia, PA 19104, USA

C. S. Chen
Department of Biomedical Engineering, Boston University,
36 Cummington Mall, Boston, MA 02215, USA

C. S. Chen
Wyss Institute for Biologically Inspired Engineering, Harvard
University, 3 Blackfan Circle, Boston, MA, USA

1 Introduction

Biological tissues are often mechanically anisotropic. This anisotropy is essential for proper tissue functioning. In the field of tissue engineering, it is therefore necessary to be able to control the anisotropy of engineered neo-tissues. The orientation of cells and their cytoskeletal F-actin stress fibers strongly influences the mechanical anisotropy of tissues. This is both a direct effect, with cells being stiffest in their longitudinal direction (Hu et al. 2004) and an indirect effect, with cells producing a collagen matrix parallel to their orientation (Birk and Trelstad 1984; Wang et al. 2003). One factor influencing cell and stress fiber orientation is their mechanical environment. When cells are embedded in a gel under static loading conditions, their stress fibers are known to orient preferably in directions in which the gel is constrained, both uniaxially (Chiron et al. 2012; Foolen et al.

2012; Henshaw et al. 2006; Nieponice et al. 2007) and biaxially (Foolen et al. 2012; Gauvin et al. 2011), leading to a clear anisotropic fiber distribution for uniaxially constrained tissues, or a random fiber orientation for biaxially constrained tissues. In biaxially constrained dynamic conditions, cells tend to avoid cyclic strain (Foolen et al. 2012; Gould et al. 2012) unless contact guidance dictates otherwise (Foolen et al. 2012), while in uniaxially constrained dynamic conditions, cellular stress fibers align in the constrained direction, independent of cyclic strain (Gauvin et al. 2011; Nieponice et al. 2007). It may be possible to induce a preferred direction and degree of cell and stress fiber orientation, as well as tissue anisotropy, by applying appropriate mechanical boundary conditions. A computational model describing how stress fibers orient in response to their mechanical environment can be of great use in determining what these boundary conditions are. Several authors have proposed a model to do this, including Deshpande et al. (2006), Zemel et al. (2010) and ourselves Obbinksps-Huizer et al. (2014). Our model qualitatively predicts stress fiber orientation in response to a range of mechanical stimuli with a single parameter set, including strain avoidance in response to cyclic strain and a preferential alignment in a constrained direction, independent of applied cyclic strain (Obbink-Huizer et al. 2014). In the current paper, we aim to quantitatively validate the stress fiber orientations predicted by our computational model for static boundary conditions. This requires simulating suitable experimental data and comparing experimental and simulated results. Ideally, these experimental data are obtained in a controlled environment that is locally heterogeneous, to validate the response of the model to different mechanical environments as well as the interaction between different regions. Previously, an experimental system to investigate the response of cells to different mechanical stimuli was developed, consisting of posts constraining initially square tissues (Foolen et al. 2012). These posts are either located along all edges of the square (biaxial constraint) or in two opposite rows (uniaxial constraint). The mechanical environment in this system is expected to be heterogeneous, in part because boundary conditions are applied to the tissues via discrete posts and not via a continuous constraint. Another interesting system to investigate the interaction between cells and their mechanical environment is the one proposed by Legant et al. (2009), in which two or four small cantilevers constrain a microscale tissue. The small size allows visualization of the entire construct and allows for high-throughput applications, while the deformation of the cantilevers with known bending stiffness quantifies tissue contraction. The small scale is also expected to increase the relevance of heterogeneity within the tissue. In this paper, we combine both systems to obtain small scale tissues that are either uniaxially or biaxially constrained by deformable posts, providing a controlled but heterogeneous mechanical environment in a newly developed high-throughput system. Investigating stress fiber orientation throughout the constrained plane in microtissues allows us to validate the computational model and, additionally, provides data on the heterogeneity of the stress fiber orientation within constrained microtissues. Furthermore, by using two different post heights, corresponding to different post bending stiffnesses, the variety of mechanical environments for the assessment of experimental heterogeneity and the validation of the computational model is increased.

2 Experimental method

2.1 Experimental model system

Adapted versions of the model system by Legant et al., containing microtissues anchored to posts positioned in four corners (Legant et al. 2009), were created (Fig. 1). In our system, post geometry and fabrication method were identical to that of Legant et al. (2009). An array of 8 by 8 microwells was created, containing either a biaxial (12 posts, Fig. 1d) or uniaxial (8 posts, Fig. 1e) setup, consisting of high (200 μm) or low (125 μm) posts. In short, multilayered masters were manufactured by photopatterning SU-8 photoresist (Microchem) on silicon wafers, via successive spin coating, UV exposure, alignment and baking. Exposure and alignment were performed on a Karl Suss MJB3 mask aligner (Suss Microtec). The masters were developed using propylene glycol methyl ether acetate (PGMEA, Sigma) and were subsequently hard baked. Poly(dimethylsiloxane) (PDMS, Sylgard 184, Dow Corning) replicates were created in a petri dish containing an 0.18 μm thick glass bottom, via an intermediate PDMS casting step to create a substrate. During replication steps, the SU-8 master and PDMS substrate were rendered non-adhesive via plasma treatment (oxygen, 1 min at 100 Watt) and overnight silanization with (trideca-fluoro-1,1,2,2-tetrahydrooctyl)-1-trichlorosilane under vacuum. During a second plasma treatment step, PDMS templates were made hydrophilic. Templates were sterilized by treatment with 70 % alcohol for 30 min and UV exposure for 15 min. Templates were treated for 2 min with 0.2 % Pluronic F127 (BASF) to reduce cell adhesion.

2.2 Microtissue seeding

Vascular-derived cells (HVSC, passage 6), characterized as myofibroblasts (Foolen et al. 2012) were suspended in growth medium (DMEM advanced, 10 % FBS, 1 % penicillin/streptomycin, 1 % glutamax, 260 μg/mL ascorbic acid). Subsequently, a gel mixture of growth medium, collagen type I (final concentration 1 mg/mL, rat tail, BD Bioscience) and sodium hydroxide, to neutralize the pH of the acidic collagen, was produced in which HVSCs were suspended to obtain a final cell concentration of 14×10^6 HVSCs per mL.
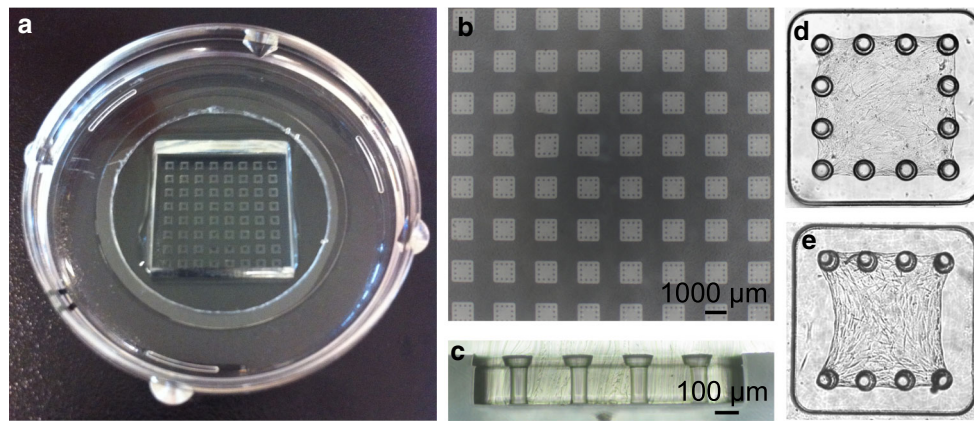
Fig. 1 Microtissue model system. **a** PDMS templates were adhered to a petri dish containing a glass bottom. **b** *Top view* of the 8 × 8 array of microwells; a black pigment was added to the PDMS for a clear overview. **c** *Side view* of 4 posts from one microwell. Post diameter was 75 μm at the base and 125 μm at the *top*, with a total height of 200 μm or 125 μm. **d** Biaxially constrained microtissue in a single well of 1125 × 1125 μm. After contraction, the tissues are approximately 800 × 800 μm. **e** Uniaxially constrained microtissue

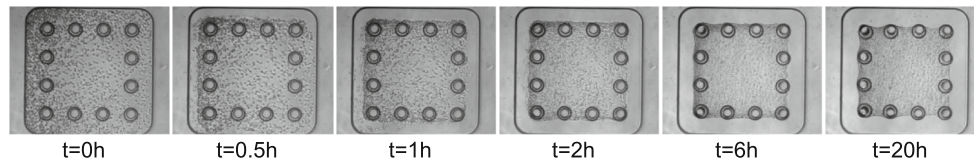| t=0h | t=0.5h | t=1h | t=2h | t=6h | t=20h |

Fig. 2 Time span of tissue contraction. Within 6 h of culturing, the tissue is fully anchored around the posts

To each microwell, approximately 0.16 μL (low posts) or 0.25 μL (high posts) of the cell-gel mixture was pipetted. The microwells were thereby fully submerged. During this procedure, the microwells were kept on ice to prevent evaporation of the gel. Gel seeding was facilitated by making the PDMS hydrophilic in the plasma oxidizer, as previously mentioned. Gels subsequently polymerized in an incubator at 37 °C, 5 % CO_2 for 10 min. To prevent dehydration of the gel, the petri dish was inverted and sterile water was added to the lid. Subsequently, growth medium was added to the microtissue constructs, which contracted around the posts within 6 h (Fig. 2).

2.3 Visualization

After 24 h of culturing, microtissues were fixed in 10 % formalin for 30 min and permeabilized for 30 min in 0.5 % Triton-X in PBS. Microtissues were incubated with phalloidin-Atto 488 (1:100 Sigma) for 30 min at room temperature to visualize F-actin. Fluorescent images were taken with a confocal microscope (Zeiss LSM 510 META NLO, Darmstadt, Germany). The excitation source was an Argon laser (488 nm). The pinhole of the photo-multiplier was set at 8 μm. The photo-multiplier accepted a wavelength region of 500–550 nm. No additional image processing was performed. Laser light was focused on the microtissues with a water immersed Achroplan 40 × /0.8 NA long distance

objective, connected to a Zeiss Axiovert 200 M. Microtissues were visualized through the glass bottom of the petri dish, while the microtissues were still anchored around the posts. Tile scans were produced composed of 4 × 4 individual images, each individual image measuring 225 × 225 μm. 2D tile scans were taken at halfway the thickness of the tissue. For each condition (biaxial or uniaxial constraint with high or low posts), five to seven tissues were scanned.

2.4 Image analysis

The tile scans showing F-actin fibers throughout the tissues were automatically cropped and divided into four equally sized quarters. These quarters were flipped based on symmetry so that all quarters had the orientation of the quarter in the left top corner. The quarters were divided into four by four equally sized subregions. The F-actin fiber distribution was determined per subregion in a manner comparable with Frangi et al. (1998), originally developed to segment clinical images of blood vessels. The implementation of the algorithm is based on Foolen et al. (2012) and de Jonge et al. (2013). In brief, a measure of "vesselness" (termed "fiberness" here) is calculated for each point in the image, based on the eigenvalues and eigenvectors of the Hessian matrix of the image intensity (second order derivative). However, in this case the interest is not in a binary value whether or not a vessel or fiber is present on a specific position but

in an overall fiber distribution. Therefore, we calculated a histogram of the amount of fibers per direction, where the contribution of the fiber direction at each pixel is weighed with its "fiberness." Hereby pixels with fiberness close to one, having a high likelihood of belonging to a fiber, strongly contribute to the final histogram, while pixels with a fiberness close to zero have a limited contribution. Pixels with a fiberness below 0.14 were excluded from the histogram, because they could occur without a preferred orientation. Initial trials showed this weighing method increased the smoothness of the histogram, with little influence on the main fiber orientation found, as compared to using a cut-off to determine whether or not a pixel(orientation) belongs to a fiber. A more detailed description of the image processing algorithm is provided in Online Resource 1. Per subregion the histograms calculated in this manner were summed for all four quarters. This resulted in a total of 16 histograms per image, that were each normalized to have a total weighed amount of fibers of hundred percent. Mean and standard deviation for each point in this series of histograms was then determined over all images corresponding to the same condition (uniaxial or biaxial constraint with high or low posts). From the resulting mean fiber fraction (FF_θ) per direction θ, the direction with largest fiber fraction ($\theta_{\max FF}$) was determined, along with the strength of alignment around this direction quantified via order parameter S (based on (Zemel et al. 2010), defined as

$$S = \frac{\sum_\theta FF_\theta \cos(2(\theta - \theta_{\max FF}))}{\sum_\theta FF_\theta}. \tag{1}$$

Three regions were defined per tissue (around posts, free edge and central region, shown in Fig. 7a, b). For each type of constraint and post height, $\theta_{\max FF}$ and S were averaged over the subregions within these regions. As a measure of the force applied by the cells to the posts, the displacement of the posts was determined from the tile scans. The locations of the posts were visible as circular regions without actin staining along the tissue edges. A circle was manually fitted for each post, and the displacement of these circles relative to the designed initial configuration was determined. These displacements were divided in a component parallel and a component perpendicular to the edge, so two displacement values per post per tissue were obtained. Of these 24 (biaxial) or 16 (uniaxial) displacement values per tissue, only 3 (biaxial) or 4 (uniaxial) were expected to be distinct based on symmetry (shown in Fig. 6b, e) and all indistinct displacements were averaged.

3 Computational method

3.1 Computational model

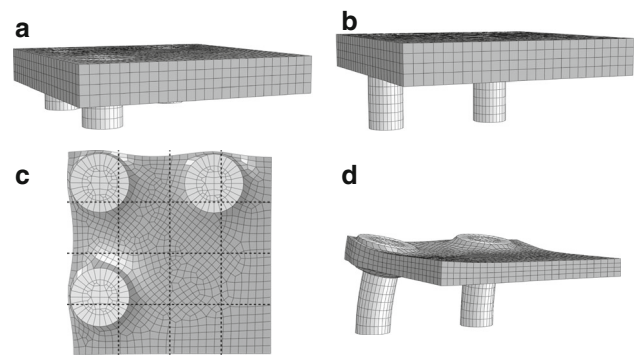The experiments were simulated via finite element analysis, using the commercial finite element package ABAQUS

Fig. 3 Overview of computational model geometry. Undeformed geometry (**a**, **b**) and deformed geometry (**c**, **d**) for biaxially constrained tissue with low posts (**a**, **c**) or uniaxially constrained tissue with high posts (**b**, **d**). In a *top view* of the model (**c**) the division in subregions is shown

(SIMULIA, Providence, RI, USA). The geometry of the entire experimental model system was modeled as a single part, divided into regions to represent the microposts and the cell-populated gel. Only a quarter of the construct was modeled for reasons of symmetry. The dimensions and spacing of the posts correspond to those in the experimental designs. Cells in the relatively large area outside the posts sense hardly any mechanical resistance and undergo extreme deformations. To avoid numerical difficulties arising from these extreme deformations, the simulated initial cell-populated gel geometry was reduced in size compared with the experimental microwell size. The gel was modeled as a cuboid around the tops of the microposts, with 20 µm of gel below and to the sides of the tops of the posts (Fig. 3). Four versions of the model were made, corresponding to the uniaxial and biaxial constraint with high or low posts. Linear hexahedral reduced integration elements were used for the microposts and linear hexahedral elements with full integration were used for the gel. A compressible neo-Hookean material model with a Young's modulus (E) of 1MPa (representative for PDMS (Jungbauer et al. 2008) and a Poisson's ratio (ν) of 0.45 was used to simulate the microposts. The cell-populated gel was modeled as a combination of a cell component, a fibrous collagen component and an isotropic component, all sharing the same mesh. Our previously developed computational model (Obbink-Huizer et al. 2014) was used to simulate the cells inside the gel. In brief, in this mechanical model cell stress is determined by a homogenization of the stress in stress fibers in a number of discrete directions. The total stress (σ^{cell}) in all fibers in a direction $\mathbf{e}_\theta$ is a weighed (weighting factor w_θ) combination of the amount of fibers in this direction (parameterized as stress fiber volume fraction Φ_θ^p) and the stress fiber stress in this direction σ_θ^p:

$$\sigma^{\text{cell}} = \sum_\theta w_\theta \, \Phi_\theta^p \, \sigma_\theta^p \, \mathbf{e}_\theta \mathbf{e}_\theta \tag{2}$$

Table 1 Material parameters

Parameter	Description	Value
$\sigma_{\max}$	Maximal stress fiber stress	$2.0e^{+5}$ Pa
ε_0	How quickly contraction reduces as strain increasingly differs from 0	$1.2e^{-1}$
ε_1	Passive strain hardening	$1.7e^{-1}$
k_v	How quickly contraction reduces as rate of shortening increases	$5.0e^{+1}$ s
k_0^f	Basal stress fiber formation	$1.5e^{-6}$ s^{-1}
k_1^f	Stress dependent stress fiber formation	$7.0e^{-7}$ s^{-1} Pa^{-1}
k_d	Stress fiber dissociation	$1.0e^{-3}$ s^{-1}
Φ^{tot}	Total actin volume fraction	$5.0e^{-2}$

This stress fiber stress is based on a Hill-type muscle model, where stress is a function of the strain ε (active component $f_{\varepsilon,a}$ plus passive component $f_{\varepsilon,p}$) and the strain rate $\dot{\varepsilon}$ (function $f_{\dot{\varepsilon}}$) according to the following:

$$\sigma_\theta^p = \sigma_{\max} f_{\dot{\varepsilon}}(f_{\varepsilon,a} + f_{\varepsilon,p}) \tag{3}$$

$$f_{\varepsilon,a} = \exp^{-(\frac{\varepsilon_\theta}{\varepsilon_0})^2} \tag{4}$$

$$f_{\varepsilon,p} = \begin{cases} 0 & \text{if } \varepsilon_\theta < 0 \\ (\frac{\varepsilon_\theta}{\varepsilon_1})^2 & \text{if } \varepsilon_\theta \geq 0 \end{cases} \tag{5}$$

$$f_{\dot{\varepsilon}} = \frac{1}{1 + \frac{2}{\sqrt{5}}}\left(1 + \frac{k_v\dot{\varepsilon}_\theta + 2}{\sqrt{(k_v\dot{\varepsilon}_\theta + 2)^2 + 1}}\right) \tag{6}$$

A high active stress fiber stress in a direction leads to a large amount of fibers (large stress fiber volume fraction) in this direction according to the following:

$$\frac{d\Phi_\theta^p}{dt} = (k_0^f + k_1^f \sigma_{\max} f_{\varepsilon,a} f_{\dot{\varepsilon}})\Phi^m - k_d \Phi_\theta^p \tag{7}$$

Furthermore, the total amount of actin, present as either monomer (Φ^m) or fiber (Φ_θ^p for angle θ) is constant according to the following:

$$\Phi^{\text{tot}} = \Phi^m + \sum_\theta w_\theta \Phi_\theta^p \tag{8}$$

The model parameters were unchanged compared with our previous publication (Obbink-Huizer et al. 2014) and are given in Table 1. Under static conditions, stress fibers mainly develop in directions where they sense large mechanical resistance using this model, as strain is low, and therefore, stress is high in such directions. In an extension to our previous work, the discrete fiber directions used, were implemented in 3D and not 2D, with the initial discrete fiber orientations and corresponding weighting factors (w_θ) determined by Lebedev quadrature points (Lebedev and Laikov 1999). Since every Lebedev point has a "partner" with the same ori-

entation but opposite direction, only half of the Lebedev grid points are used, in this case 25 orientations, while the weighting factors of both directions are summed. Fibrous collagen was taken into account in the same discrete directions as the stress fibers. The total stress due to all fibrous collagen was a homogenization of the stress in these directions, taking into account the collagen fiber volume fraction, which was 0.02 in all directions. The collagen fibers were assumed to only contribute to stress in extension and an exponential stress-extension ($\sigma - \lambda$) relationship was used:

$$\sigma = \begin{cases} 0 & \text{if } \lambda < 1 \\ k_1\lambda^2(\exp^{k_2(\lambda^2-1)} - 1) & \text{if } \lambda \geq 1 \end{cases} \tag{9}$$

with k_1 and k_2 taken as 0.676 and 2.75, respectively (Driessen et al. 2007). The relatively small influence on tissue mechanical properties of other factors than the ones explicitly taken into account, such as non-contractile cell components and possibly glycosaminoglycans (GAGs), is combined into a single isotropic component, modeled as a low stiffness ($E = 50$ Pa, $\nu = 0.2$) neo-Hookean material. This provides some resistance to compression and stabilizes the material. For each of the four model versions, a simulation was run for 10000 s. During this period, an equilibrium stress fiber distribution had developed starting from an initial situation without stress fibers.

3.2 Computational model data analysis

To compare experimental and computational results, the output from the simulations—per element the deformation and the stress fiber volume fraction for each direction—is converted to a series of 4×4 subregion histograms for each case (biaxial or uniaxial with high or low posts). To obtain 2D histograms from the 3D data, the stress fiber volume fractions in the four directions originally in the horizontal plane are considered. Because the number of directions precisely in the horizontal plane is limited, directions under a small angle with respect to the horizontal plane are also included: four directions above the plane (18°) and these four directions mirrored in the plane. Stress fiber volume fractions and initial fiber orientations of mirrored points are averaged, so a total of eight fiber directions and corresponding volume fractions were taken into account per element. The density of discrete fiber directions changes as fibers deform with the material (Fig. 4). To take this into account, directions initiallyhalfway between neighboring fiber directions were defined (gray in Fig. 4). The stress fiber volume fraction in each direction was then divided by the ratio of the deformed angle between the two halfway directions neighboring the fiber direction to the initial angle between the two halfway directions neighboring the fiber direction. The result is termed the "scaled stress fiber volume fraction." This scaled stress fiber frac-
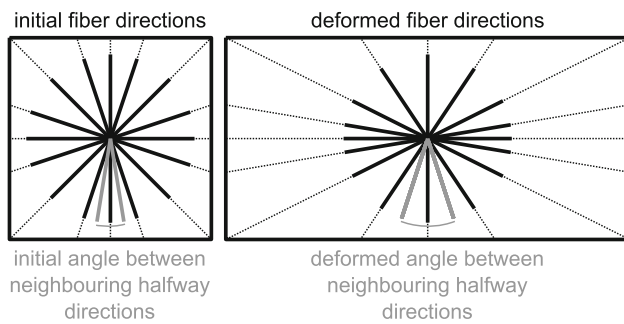
Fig. 4 Change in discrete fiber density due to deformation. If there is more extension in one direction than in the other, as depicted here, fiber directions will rotate with the material so the fiber direction density in the most extended direction is increased and fiber direction density in the least extended direction is reduced. To take into account the influence of fiber direction density on fiber fraction, the calculated fiber volume fraction per direction is divided by the ratio of the deformed to the initial angle between the two neighboring halfway fibers. These angles are indicated in the figure for one representative discrete fiber direction
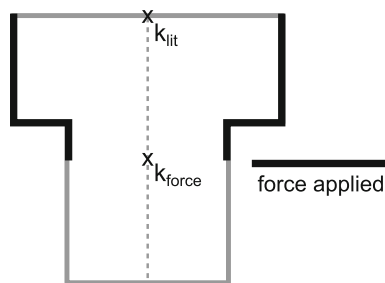

Fig. 5 Cut through micropost illustrating bending stiffness calculation. A force is applied equally distributed over the region in contact with the gel when simulating experiments (*thick black line*). Post displacement is determined at two different locations, to calculate two measures of bending stiffness. Both locations are indicated by an "x" and each is marked with the corresponding stiffness measure

tion was linearly interpolated between the deformed fiber orientation angles in the horizontal plane to obtain a histogram. The elements were divided into 4×4 same sized subregions, depending on their deformed coordinates (Fig. 3c). The histograms of all elements belonging to the same subregion were summed and afterward normalized to have a total value of hundred percent. These are compared with the experimental results. For simulated results $\theta_{\max FF}$ and S where determined in the same manner and for the same regions as was done for experimental results, and for each case (biaxial or uniaxial with high or low posts), average values over the different regions (between posts, along free edge, central region) were compared with the corresponding experimental values. To compare the force applied by the cells to the posts in experiment and simulation, for each post, the displacement of the node in the center of the first horizontal layer below the wider top was determined (indicated by k_{force} in Fig. 5). This location was chosen because in most cases, the diameter of the experimentally found post circles was 75 µm, the diameter of the base of the post. To estimate the bending stiffness

of both a high and a low post, an in time linearly increasing force was applied to each of the posts, evenly distributed over the post surface in contact with the gel when simulating the experiments, corresponding to the entire circumference of the post (Fig. 5). Post stiffness was then calculated as the applied force divided by the post displacement in the initial, linear, region. This was done for two measures of displacement: the displacement of the node in the center of the top surface of the post and the displacement of the node in the center of the first horizontal layer below the wider top. Bending stiffness values were termed k_{lit} and k_{force}, respectively, as the first stiffness measure is expected to be comparable with literature (including (Legant et al. 2009)), while the second measure can be used to estimate the force on the posts from the determined displacement.

4 Results

4.1 Experimental results

For all conditions (biaxial or uniaxial with high or low posts) close to the posts, stress fibers were mainly oriented between neighboring posts (Fig. 6b, d). In the biaxially constrained tissues in the 3×3 subregions not containing posts, there was no dominant orientation and little difference between different subregions (Fig. 6b). In the center of the uniaxially constrained tissues, stress fibers were mainly oriented in the constrained direction (0/180°). Approaching the free edge of the tissue, the preference became stronger with a main orientation parallel to the free edge. Toward the posts, the preference for the constrained direction reduced (Fig. 6d). Results for high and low posts were generally comparable, though in the case of high posts, there was a stronger preference for a single direction in between posts. These effects are also reflected in $\theta_{\max FF}$ and S (Fig. 7): in regions U1 and B1, and B2, which contain the posts, $\theta_{\max FF}$ is 90 or 180°, respectively, corresponding to the direction between neighboring posts (Fig. 7c, d). In the center of the biaxially constrained tissue (B3) S and thus alignment strength is low (Fig. 7f). In the center of the uniaxially constrained tissue (region U3), $\theta_{\max FF}$ is close to 180° (the constrained direction, Fig. 7c) and S is smaller than the S close to the free edge (region U2), showing alignment strength is less (Fig. 7e). $\theta_{\max FF}$ was similar in high and low posts, showing the main orientation agreed, while S differed for the post containing regions U1, B1 and B2, showing the strength of this preference differed.

4.2 Computational results

Computed and experimental stress fiber distributions agreed well for both the uniaxial and biaxial constraint (Fig. 6b, d). Comparable with experimental results, the simulations
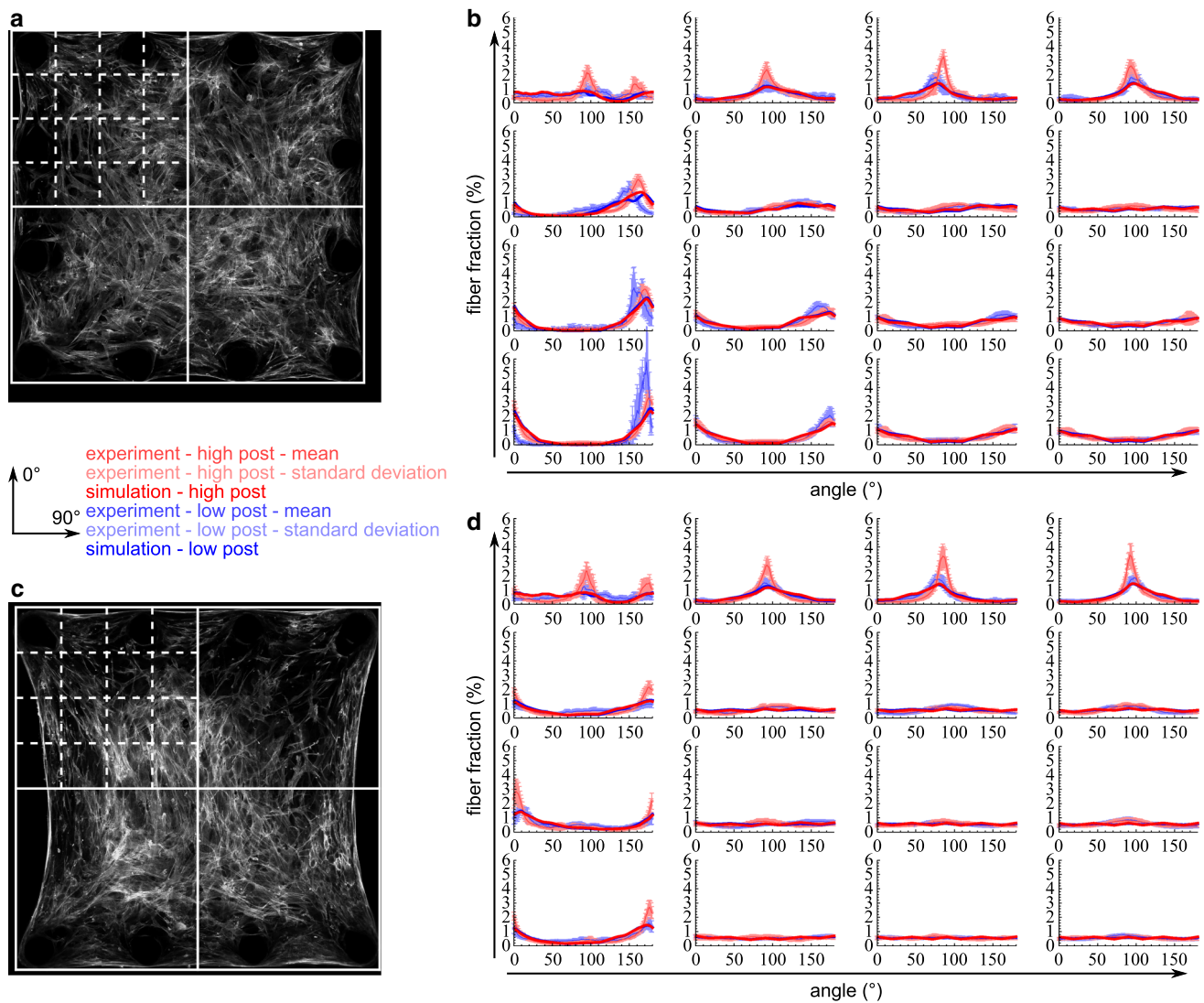
Fig. 6 Experimental and simulated results. Representative experimental fluorescent image of F-actin stress fibers, with top left corner divided into subregions (**a**, **c**). Histograms showing fiber distribution per subre-gion (**b**, **d**). The arrangement of these histograms corresponds to the grid shown in the top left corner of the representative fluorescent images. A biaxial (**a**, **b**) or uniaxial (**c**, **d**) constraint is applied

showed a preferred orientation between neighboring posts, a large homogeneous and randomly oriented central region for the biaxially constrained tissues and a more heterogeneous stress fiber orientation for uniaxially constrained tissues, with a preferred orientation in the constrained direction or along the free edge. Differences between high and low posts were small in the simulations, as was the case experimentally. The largest discrepancies between experiment and simulation occurred near the posts and along the free edge of the uniaxially constrained tissues. In the numerical simulations, the preference for a specific direction was weaker and no difference between the high and low posts was observed in these regions. Outside these areas, the simulated fiber fraction was almost always within the standard deviation of the experimental mean, indicating quantitative agreement between experimental and simulated results. Again $\theta_{\max FF}$

and S values confirm the results shown in the histograms. For $\theta_{\max FF}$, simulated and experimental mean $\pm$ standard deviation regions overlap for all regions except B3. In this region, alignment is limited, as indicated by a small S, which explains the difference in $\theta_{\max FF}$. Mean simulated S is within a standard deviation of the mean experimental S for the uni-axial free edge and central regions (U2 and U3), but not in the regions containing posts (U1, B1 and B2) as expected based on the histograms (Fig. 6b, d). Mean simulated S is more than a standard deviation lower than the mean experimental S in the biaxial central region (B3). Because experimental and simulated histograms are comparable in this region and no preferred orientation is expected based on symmetry considerations, we expect this difference is due to noise on the experimental data, and does not reflect an inaccuracy in the model. Post displacement, which is related to the force
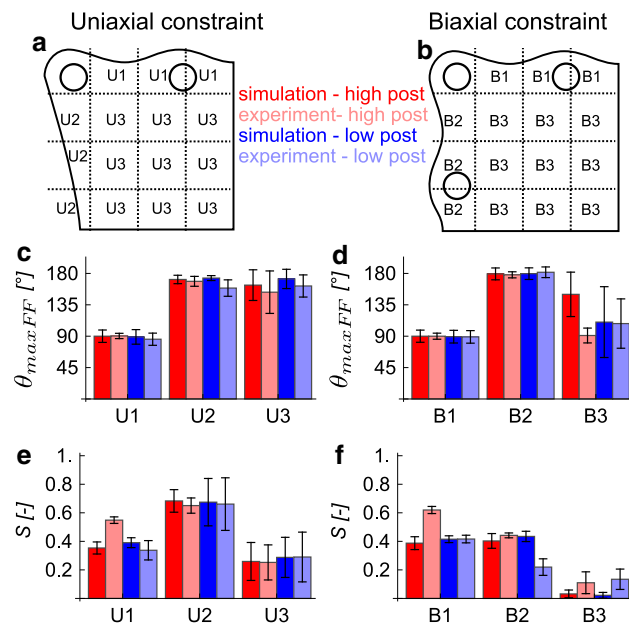
Fig. 7 Experimental and simulated stress fiber distributions quantified via θ_{maxFF} and S for different regions. Division in regions is shown for uniaxial constrain (**a**) and biaxial constraint (**b**) and results are shown per parameter (θ_{maxFF} (**c**, **d**) and S (**e**, **f**)) and constraint type (uniaxial(**c**,**e**) and biaxial (**d**, **f**))
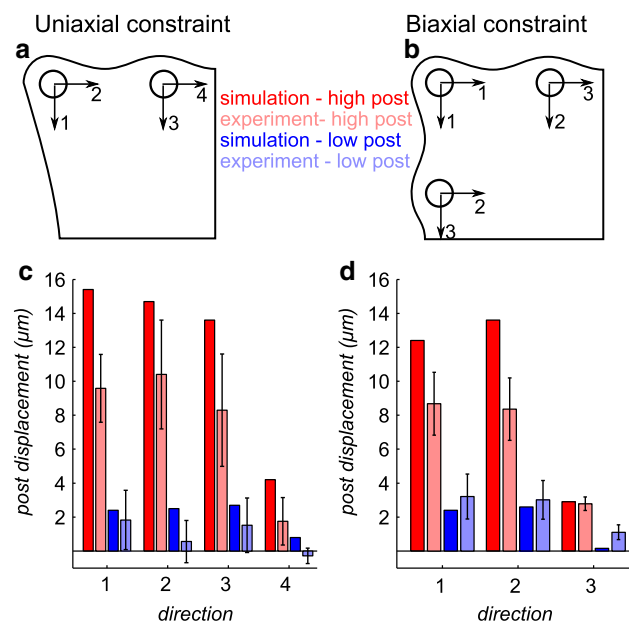

Fig. 8 Comparison of simulated to experimental displacements. Definition of directions used to determine displacement for uniaxial (**a**) or biaxial (**b**) constraint. Micropost displacement for uniaxial (**c**) or biaxial (**d**) constraint including standard deviation over different images for experimental data. This displacement is related to the force applied by the cells in the tissue construct to the posts via post stiffness, which differs between high and low posts

applied by the cells in the tissue construct to the posts via post stiffness, was taken into account in the directions indicated in Fig. 8a, b. Trends in post displacement were sim-

ilar in experiment and simulation. For both simulation and experiment, displacement was larger for high posts than for low posts, as expected due to the lower bending stiffness of high posts. For all conditions, post displacement was smallest for the non-corner post in the direction parallel to the edge (direction 3 (biaxial) or 4 (uniaxial) in Fig. 8a or b). Displacement in the other directions was approximately equal in most cases. Quantitatively, most of the simulated displacements were larger than the corresponding experimentally observed displacements, but the order of magnitude agreed. The k_{lit} and k_{force} of the high post were 0.8 and 1.4 μN/μm, respectively, while the low post had a k_{lit} of 3.6 μN/μm and a k_{force} of 11 μN/μm.

5 Discussion

5.1 Main findings and implications

We aimed to quantitatively validate our computational model, describing stress fiber orientation in response to the mechanical environment. In this model, we assume stress fibers mainly develop in directions in which they can apply high stress, i.e., in directions in which strain and shortening rate are small, even if stress fibers actively try to contract. These are the directions in which the cell senses a large resistance to deformation. When simulating microtissue experiments with our computational model using the same material parameters that were used previously, we found a simulated fiber fraction that was within the standard deviation of the experimentally observed mean throughout most of the mid-plane of the tissue for each of the four conditions investigated (uniaxially or biaxially constrained with high or low posts). When comparing the experimental and simulated displacements, there was qualitative agreement and the orders of magnitude were the same. The agreement between experimental and simulated results supports our hypothesis on stress fiber orientation, as formulated in the model. It indicates that stress fiber orientation in these microtissues is mainly determined by the mechanical environment, and not by, e.g., contact guidance, because our mechanics-based model accurately predicts stress fiber orientation. Because of this good agreement, we suggest that our model can be used to predict stress fiber distributions without the necessity of large amounts of experimental studies, provided mechanical boundary conditions are known. Currently, this is especially the case for static conditions when using comparable tissue constructs, because these conditions have been most extensively validated so far.

Additionally, our experiments provide new evidence on how stress fibers orient in microtissues, including the heterogeneity of stress fiber orientation in these microtissues, while the combination of experimental data with the compu-

tational model provides an explanation of why stress fibers orient the way they do. Our experimental results show that the stress fiber orientation is approximately random in biaxially constrained tissues. According to the model, this occurs because cells sense a similar resistance to deformation in all directions in the constrained plane. Between neighboring posts the cells are effectively uniaxially constrained by the posts, and respond accordingly. In our model, this happens because cells sense a much larger resistance to deformation in the direction between the posts, than in the perpendicular, free, direction and therefore orient in the direction between the posts. Apart from the subregions containing the posts, no consistent differences between the subregions were found. In the light of our model, this implies resistance to deformation is constant in this region. This homogeneity also indicates that using an off-center or larger image to determine fiber orientation in the biaxially constrained system will not influence results as long as no micropost is directly included in the image used. In the uniaxially constrained tissue, stress fibers develop preferably in the constrained direction, which, according to our model, is due to the increased resistance to deformation in this direction. The stress fiber distribution in the uniaxially constrained tissues is more heterogeneous than in the biaxially constrained tissue. The preferred cell orientation in subregions close to the free edge is more pronounced, while subregions closer to the posts have a less pronounced preferred orientation compared with the center. At the free edge, resistance to deformation is high along the edge, while the material is almost free to deform perpendicular to the edge. In the center of the uniaxially constrained constructs the difference in resistance between constrained and perpendicular direction is smaller, because in this region the posts provide more resistance to compaction in the perpendicular direction. According to the model, this leads to less pronounced alignment. Closer to the posts, the posts provide even more resistance to compaction, and alignment is further reduced. The preferred direction also changes: from approximately 180° in the center, to 150° (low posts) or 165° (high posts) near the corner post, reflecting a change in the direction of most resistance. Results are thus influenced by the subregion where they are determined in this uniaxially constrained case and this should be taken into account when performing experiments. Also, as the uniaxially constrained microtissues are more anisotropic near the edge, this may be exploited when attempting to develop anisotropic tissues, e.g., by changing the length-width ratio to increase the amount of edge and possibly anisotropy. To test whether an increased tissue length can indeed increase tissue anisotropy, we used our model to predict the stress fiber distribution in a tissue with a twice as high length in constrained direction as the standard simulation. Main stress fiber orientations were similar in the long and the standard tissue. In the center of the construct, the preference for the constrained direction

was stronger in the long tissue than in the standard tissue, as expected ($S = 0.6$ in long tissue and 0.2 in standard tissue). In general, this was the case throughout the tissue. However, at the free edge alignment was more pronounced in the standard tissue ($S = 0.7$ at the center of the free edge) than in the long tissue ($S = 0.6$ at the center of the free edge). Apparently, the greater distance to the posts in the long tissue allows a constant alignment strength between construct center and free edge center, while in the standard simulation, the proximity of the posts limits the compaction and therefore alignment at the construct center, while increased compaction is allowed at the free edge, partly due to the presence of tissue material outside the posts. Overall, increasing the tissue length homogenizes the stress fiber distribution around the center of the construct and increases alignment strength except at the free edge. An increased tissue length may therefore be beneficial when attempting to engineer anisotropic tissue constructs.

In general, post height had a limited influence on stress fiber orientation in the range that was tested (125 vs. 200 μm). In the model, competition between direction causes stress fibers to align based on differences in sensed resistance, and not based on absolute resistance. This may explain the limited influence of post height on stress fiber orientation in general. However, higher posts led to a stronger preference for a single fiber direction between posts and, for the uniaxially constrained tissues, a preferred fiber orientation closer to 180° near the corner post. Both effects are consistent with increased compaction for low compared with high posts.

5.2 Comparison with literature

The experimental microtissue approach used in the current work is similar to the one described by Legant et al. (2009). (Legant et al. 2009) reported an increase in microtissue tension for cantilevers of increased stiffness. When multiplying the displacement of the posts with the corresponding k_{force} values, we also found an increased force perpendicular to a constrained edge for higher bending stiffness. So, while post stiffness had a limited influence on our main outcome of stress fiber orientation and both bending stiffnesses used in this work are higher than those used by Legant et al. (2009), the bending stiffness difference investigated here was large enough to influence tissue tension.

Legant et al. (2009) also investigated actin orientation and alignment, both experimentally and computationally. As in the current work, actin aligned parallel to free edges, with strongest alignment close to the edges, experimentally and computationally. Due to differences in post geometry between Legant et al. (2009) and this work, local actin alignment differed. Notably, a homogeneous region was present in our biaxially constrained tissues, which had additional posts along the edge compared with the four cantilever

setup described by Legant et al. (2009). This homogeneous region, not present in the four cantilever setup, could be valuable when investigating the influence of other factors than mechanical constraints on cell orientation. When comparing the computational modeling approaches, the model used to describe actin fiber development is based on Deshpande et al. (2006) in Legant et al. (2009), while actin fiber development in the current work is based on Obbink-Huizer et al. (2014). In both models stress fibers mainly develop in directions in which a large resistance to deformation is sensed, but the mechanism by which this is sensed differs: in Deshpande et al. (2006) a low resistance to deformation is sensed as a history of a high fiber shortening rate, while in Obbink-Huizer et al. (2014) a low resistance to deformation is sensed as a large instantaneous negative strain. This different approach influences the versatility of the model to predict the stress fiber distribution, especially in response to mechanical environments with both dynamic strain and an anisotropic resistance to deformation (Obbink-Huizer et al. 2014). Furthermore, unlike Legant et al. (2009), in the current model the post geometry is explicitly taken into account, fiber directions are defined in three dimensions and a fibrous collagen component is included.

5.3 Experimental limitations

In some of the images of uniaxially constrained tissues with low posts, part of the tissue was out of focus, so no fibers could be detected. This mainly occurred along the free edges of the tissue and may be due to the attachment height of the tissue to the post. In the subregion corresponding to the center of the free edge, where data are already limited due to the compaction of the tissue, no fibers were found for some images. In another case, only a small amount of fibers were found. If these were to be normalized and averaged with the rest of the data, these few fibers would have dominated results. Therefore, in the mean histogram corresponding to each subregion, only histograms with a total weighed fiber fraction above 5 before normalization were included. We expect this missing data to have limited influence on the mean cell orientation, because it affects fibers independent of their orientation. In the future, in focus images of each part of the tissue can be made by scanning at different depths (3D). We expect this to reduce the standard deviation of the two subregions at the center of the free edge of the uniaxially constrained low-post microtissue, while having little influence on all other results. Therefore, we do not expect an influence on our conclusions.

5.4 Computational limitations

The largest discrepancies between experimentally observed and simulated fiber orientation occurred near the microposts and along the free edge of the uniaxially constrained

tissue. In these regions, the difference between experimental and simulated geometry was largest: experimentally, the cell-populated gel initially filled an entire well that was larger than the initial gel geometry taken into account in the simulation. The smaller simulated geometry may lead to reduced compaction perpendicular to the direction constrained by the posts and therefore a less pronounced preferred orientation, as seen in the simulations. Comparing post displacement in experiment and simulation provided an indication of how accurately our computational model describes the force applied by the cells to the post in the experimental model system. The order of magnitude of post displacement in experiment and simulation agreed, but overall the simulation overestimated the displacements. It may be that a difference in attachment height of the tissue to the post causes this discrepancy. In the simulations, we fixed most of the tissue to the top part of the post. Most experimental images showed a post diameter corresponding to the lower part, which might indicate the tissue was mainly fixed at a lower height than assumed in the simulations. The top of the posts requires less force to obtain the same displacement compared with the bottom of the post, which corresponds to a lower bending stiffness at the top than at the bottom of the post. A too high attachment position would result in an overestimation of post displacement in the simulations, which indeed happened in most cases. To accurately assess cell forces in similar microtissues, more detailed experiments are needed, with a more exact and full 3D analysis, including both post displacement and the location on the post where the cells apply force. This is a topic of ongoing research by our group. The difference in effective bending stiffness along the height of the posts did not cause significant differences in stress fiber orientation in different horizontal layers of the tissue, which is consistent with the limited influence of post height on stress fiber orientation that was found. The limited influence of post height on stress fiber orientation along with the more accurate prediction of cell orientation compared with post displacement (and thus force) indicate the stress fiber orientation response is relatively insensitive to changes in stiffness or force. If the tissue was indeed attached lower on the post experimentally than computationally, the true experimental bending stiffness would be higher than the values estimated here. Because uncertainties on the stiffness value lead to increased uncertainty on the force that is calculated from it, we chose to directly compare experimental and simulated deformations as a measure of the force and not the force itself. A continuum approach was taken to model the tissue, while it consists of cells and surrounding matrix, which each have an explicit geometry and interact with each other. As the length scale of the tissue ($\sim 800\,\mu\text{m}$) is larger than the size of the cells ($\sim 30 \times 90\,\mu\text{m}$) and our simulated results agree well with experimental results, we believe this approach is reasonable. However, if smaller tissues are used, a contin-

uum approach may no longer be valid. While our stress fiber model may still be applicable to the stress fibers themselves, it is likely necessary to include other cell components, such as the nucleus, explicitly. This is beyond the scope of the current work.

5.5 Conclusion

Apart from tissue edges where simulated and experimental geometry differed, we obtained good quantitative agreement between experimental and simulated local stress fiber orientations, by assuming stress fibers mainly develop in directions in which they can apply highest stress. In the microtissue system tested, highest stress could be applied in directions in which mechanical resistance was largest: in between neighboring posts, along a free edge and in constrained directions. In most parts of biaxially constrained tissues, this led to a random and homogeneous stress fiber orientation, while in uniaxially constrained tissues, it led to a heterogeneous stress fiber orientation with an overall preference for the constrained direction, both in the simulations and in the experiments.

References

Birk DE, Trelstad RL (1984) Extracellular compartments in matrix morphogenesis: collagen fibril, bundle, and lamellar formation by corneal fibroblasts. J Cell Biol 99(6):2024–2033

Chiron S, Tomczak C, Duperray A, Lainé J, Bonne G, Eder A, Hansen A, Eschenhagen T, Verdier C, Coirault C (2012) Complex interactions between human myoblasts and the surrounding 3D fibrin-based matrix. PLoS ONE 7(4):e36173. doi:10.1371/journal.pone.0036173

Deshpande VS, McMeeking RM, Evans AG (2006) A bio-chemo-mechanical model for cell contractility. Proc Natl Acad Sci USA 103(38):14015–14020. doi:10.1073/pnas.0605837103

de Jonge N, Kanters FMW, Baaijens FPT, Bouten CVC (2013) Strain-induced collagen organization at the micro-level in fibrin-based engineered tissue constructs. Ann Biomed Eng 41(4):763–774. doi:10.1007/s10439-012-0704-3

Driessen NJB, Mol A, Bouten CVC, Baaijens FPT (2007) Modeling the mechanics of tissue-engineered human heart valve leaflets. J Biomech 40(2):325–334. doi:10.1016/j.jbiomech.2006.01.009

Foolen J, Deshpande VS, Kanters FMW, Baaijens FPT (2012) The influence of matrix integrity on stress-fiber remodeling in 3D. Biomaterials 33(30):7508–7518. doi:10.1016/j.biomaterials.2012.06.103

Frangi AF, Niessen WJ, Vincken KL, Viergever MA (1998) Multiscale vessel enhancement filtering. In: Wells WM, Colchester A, Delp SL (eds) Med Image Comput Comput Interv - MICCAI'98, Springer, Berlin Heidelberg, pp 130–137, doi:10.1007/BFb0056195

Gauvin R, Parenteau-Bareil R, Larouche D, Marcoux H, Bisson F, Bonnet A, Auger FA, Bolduc S, Germain L (2011) Dynamic mechanical stimulations induce anisotropy and improve the tensile properties of engineered tissues produced without exogenous scaffolding. Acta Biomater 7(9):3294–3301. doi:10.1016/j.actbio.2011.05.034

Gould RA, Chin K, Santisakultarm TP, Dropkin A, Richards JM, Schaffer GB, Butcher JT (2012) Cyclic strain anisotropy regulates valvular interstitial cell phenotype and tissue remodeling in three-dimensional culture. Acta Biomater 8(5):1710–1719

Henshaw DR, Attia E, Bhargava M, Hannafin JA (2006) Canine ACL fibroblast integrin expression and cell alignment in response to cyclic tensile strain in three-dimensional collagen gels. J Orthop Res 24(3):481–490

Hu S, Eberhard L, Love JC, Butler JP, Fredberg JJ, Whitesides GM, Wang N (2004) Mechanical anisotropy of adherent cells probed by a three-dimensional magnetic twisting device. Am J Physiol Cell Physiol 287(5):1184–1191

Jungbauer S, Gao H, Spatz JP, Kemkemer R (2008) Two characteristic regimes in frequency-dependent dynamic reorientation of fibroblasts on cyclically stretched substrates. Biophys J 95(7):3470–3478. doi:10.1529/biophysj.107.128611

Lebedev VI, Laikov DN (1999) A quadrature formula for the sphere of the 131st algebraic order of accuracy. Doklady Mathematics 59(3):477–481

Legant WR, Pathak A, Yang MT, Deshpande VS, McMeeking RM, Chen CS (2009) Microfabricated tissue gauges to measure and manipulate forces from 3D microtissues. Proc Natl Acad Sci USA 106(25):10097–10102. doi:10.1073/pnas.0900174106

Nieponice A, Maul TM, Cumer JM, Soletti L, Vorp DA (2007) Mechanical stimulation induces morphological and phenotypic changes in bone marrow-derived progenitor cells within a three-dimensional fibrin matrix. J Biomed Mater Res A 81(3):523–530. doi:10.1002/jbm.a.31041

Obbink-Huizer C, Oomens CWJ, Loerakker S, Foolen J, Bouten CVC, Baaijens FPT (2014) Computational model predicts cell orientation in response to a range of mechanical stimuli. Biomech Model Mechanobiol 13(1):227–236 doi:10.1007/s10237-013-0501-4

Wang JHC, Jia F, Gilbert TW, Woo SLY (2003) Cell orientation determines the alignment of cell-produced collagenous matrix. J Biomech 36(1):97–102

Zemel A, Rehfeldt F, Brown AEX, Discher DE, Safran SA (2010) Optimal matrix rigidity for stress fiber polarization in stem cells. Nat Phys 6(6):468–473. doi:10.1038/nphys1613